

# Comparative spectroscopic and thermo-optic study of Tm:LiLnF<sub>4</sub> (Ln = Y, Gd, and Lu) crystals for highly-efficient microchip lasers at ~2 μm

PAVEL LOIKO,<sup>1,2</sup> JOSEP MARIA SERRES,<sup>1</sup> XAVIER MATEOS,<sup>1,3,6,\*</sup> SIMONE TACCHINI,<sup>3</sup> MAURO TONELLI,<sup>4</sup> STEFANO VERONESI,<sup>4</sup> DANIELA PARISI,<sup>4</sup> ALBERTO DI LIETO,<sup>4</sup> KONSTANTIN YUMASHEV,<sup>5</sup> UWE GRIEBNER,<sup>3</sup> AND VALENTIN PETROV<sup>3</sup>

<sup>1</sup>Física i Cristal·lografia de Materials i Nanomaterials (FiCMA-FiCNA), Universitat Rovira i Virgili (URV), Campus Sescelades, c/ Marcel·li Domingo, s/n., E-43007 Tarragona, Spain

<sup>2</sup>ITMO University, 49 Kronverkskiy pr., 197101 St. Petersburg, Russia

<sup>3</sup>Max Born Institute for Nonlinear Optics and Short Pulse Spectroscopy, Max-Born-Str. 2a, D-12489 Berlin, Germany

<sup>4</sup>NEST Istituto Nanoscienze-CNR and Dipartimento di Fisica dell'Università di Pisa, Largo B. Pontecorvo 3, 56127 Pisa, Italy

<sup>5</sup>Center for Optical Materials and Technologies (COMT), Belarusian National Technical University, 65/17 Nezavisimosti Ave., 220013 Minsk, Belarus

<sup>6</sup>mateos@mbi-berlin.de

\*xavier.mateos@urv.cat

**Abstract:** We report on a detailed comparative study of the spectroscopic and thermo-optic properties of tetragonal Tm:LiLnF<sub>4</sub> (Ln = Y, Gd, and Lu) crystals indicating their suitability for highly-efficient microchip lasers diode-pumped at ~791 nm and operating at ~1.91 μm. An *a*-cut 8 at.% Tm:LiYF<sub>4</sub> micro-laser generated 3.1 W of linearly polarized output at 1904 nm with a slope efficiency of  $\eta = 72\%$  and a laser threshold of only 0.24 W. The internal loss for this crystal is as low as 0.0011 cm<sup>-1</sup>. For 8 at.% Tm:LiGdF<sub>4</sub> and 12 at.% Tm:LiLuF<sub>4</sub> lasers, the output power reached ~2 W and  $\eta$  was 65% and 52%, respectively. The thermal lens in all Tm:LiLnF<sub>4</sub> crystals is weak, positive and low-astigmatic. The potential for the Tm:LiLnF<sub>4</sub> lasers to operate beyond ~2 μm due to a vibronic coupling has been proved. The Tm:LiYF<sub>4</sub> vibronic laser generated 375 mW at 2026–2044 nm with  $\eta = 31\%$ . The Tm:LiLnF<sub>4</sub> crystals are very promising for passively Q-switched microchip lasers.

© 2017 Optical Society of America

**OCIS codes:** (140.3380) Laser materials; (300.0300) Spectroscopy; (140.3480) Lasers, diode-pumped.

## References and links

1. S. So, J. I. Mackenzie, D. P. Sheperd, W. A. Clarkson, J. G. Betterton, and E. K. Gorton, "A power-scaling strategy for longitudinally diode-pumped Tm:YLF lasers," *Appl. Phys. B* **84**(3), 389–393 (2006).
2. M. Schellhorn, "High-power diode-pumped Tm:YLF laser," *Appl. Phys. B* **91**(1), 71–74 (2008).
3. X. M. Duan, B. Q. Yao, C. W. Song, J. Gao, and Y. Z. Wang, "Room temperature efficient continuous wave and Q-switched Ho:YAG laser double-pass pumped by a diode-pumped Tm:YLF laser," *Laser Phys. Lett.* **5**(11), 800–803 (2008).
4. M. Pollnau, P. J. Hardman, M. A. Kern, W. A. Clarkson, and D. C. Hanna, "Upconversion-induced heat generation and thermal lensing in Nd:YLF and Nd:YAG," *Phys. Rev. B* **58**(24), 16076–16092 (1998).
5. B. M. Walsh, N. P. Barnes, M. Petros, J. Yu, and U. N. Singh, "Spectroscopy and modeling of solid state lanthanide lasers: Application to trivalent Tm<sup>3+</sup> and Ho<sup>3+</sup> in YLiF<sub>4</sub> and LuLiF<sub>4</sub>," *J. Appl. Phys.* **95**(7), 3255–3271 (2004).
6. R. Faoro, M. Kadankov, D. Parisi, S. Veronesi, M. Tonelli, V. Petrov, U. Griebner, M. Segura, and X. Mateos, "Passively Q-switched Tm:YLF laser," *Opt. Lett.* **37**(9), 1517–1519 (2012).
7. C. Pfister, R. Weber, H. P. Weber, S. Merazzi, and R. Gruber, "Thermal beam distortions in end-pumped Nd:YAG, Nd:GSGG, and Nd:YLF rods," *IEEE J. Quantum Electron.* **30**(7), 1605–1615 (1994).
8. N. Coluccelli, G. Galzerano, F. Cornacchia, A. Di Lieto, M. Tonelli, and P. Laporta, "High-efficiency diode-pumped Tm:GdLiF<sub>4</sub> laser at 1.9 microm," *Opt. Lett.* **34**(22), 3559–3561 (2009).
9. N. Coluccelli, G. Galzerano, P. Laporta, F. Cornacchia, D. Parisi, and M. Tonelli, "Tm-doped LiLuF<sub>4</sub> crystal for efficient laser action in the wavelength range from 1.82 to 2.06 microm," *Opt. Lett.* **32**(14), 2040–2042 (2007).

10. B. Oreshkov, S. Veronesi, M. Tonelli, A. di Lieto, V. Petrov, U. Griebner, X. Mateos, and I. Buchvarov, "Tm<sup>3+</sup>:LiGdF<sub>4</sub> Laser, passively Q-switched with a Cr<sup>2+</sup>:ZnSe saturable absorber," *IEEE Photonics J.* **7**(3), 1502206 (2015).
11. H. Yu, V. Petrov, U. Griebner, D. Parisi, S. Veronesi, and M. Tonelli, "Compact passively Q-switched diode-pumped Tm:LiLuF<sub>4</sub> laser with 1.26 mJ output energy," *Opt. Lett.* **37**(13), 2544–2546 (2012).
12. J. J. Zayhowski, "Microchip lasers," *Opt. Mater.* **11**(2–3), 255–267 (1999).
13. J. J. Zayhowski and C. Dill III, "Diode-pumped passively Q-switched picosecond microchip lasers," *Opt. Lett.* **19**(18), 1427–1429 (1994).
14. J. M. Serres, X. Mateos, P. Loiko, K. Yumashev, N. Kuleshov, V. Petrov, U. Griebner, M. Aguiló, and F. Díaz, "Diode-pumped microchip Tm:KLu(WO<sub>4</sub>)<sub>2</sub> laser with more than 3 W of output power," *Opt. Lett.* **39**(14), 4247–4250 (2014).
15. M. Gaponenko, N. Kuleshov, and T. Südmeyer, "Passively Q-switched thulium microchip laser," *IEEE Photonics Technol. Lett.* **28**(2), 147–150 (2016).
16. P. Loiko, J. M. Serres, X. Mateos, K. Yumashev, A. Yasukevich, V. Petrov, U. Griebner, M. Aguiló, and F. Díaz, "Subnanosecond Tm:KLuW microchip laser Q-switched by a Cr:ZnS saturable absorber," *Opt. Lett.* **40**(22), 5220–5223 (2015).
17. P. Loiko, J. M. Serres, X. Mateos, H. Yu, H. Zhang, J. Liu, K. Yumashev, U. Griebner, V. Petrov, M. Aguiló, and F. Díaz, "Thermal lensing and multi-watt microchip laser operation of Yb:YCOB crystals," *IEEE Photonics J.* **8**(3), 1501312 (2016).
18. N. Hodgson and H. Weber, *Optical Resonators: Fundamentals, Advanced Concepts and Applications* (Springer, 1997).
19. B. F. Aull and H. P. Jenssen, "Vibronic interactions in Nd:YAG resulting in nonreciprocity of absorption and stimulated emission cross sections," *IEEE J. Quantum Electron.* **18**(5), 925–930 (1982).
20. S. A. Payne, L. L. Chase, L. K. Smith, W. L. Kway, and W. F. Krupke, "Infrared cross-section measurements for crystals doped with Er<sup>3+</sup>, Tm<sup>3+</sup>, and Ho<sup>3+</sup>," *IEEE J. Quantum Electron.* **28**(11), 2619–2630 (1992).
21. M. Eichhorn, "Quasi-three-level solid-state lasers in the near and mid infrared based on trivalent rare earth ions," *Appl. Phys. B* **93**(2–3), 269–316 (2008).
22. R. L. Aggarwal, D. J. Ripin, J. R. Ochoa, and T. Y. Fan, "Measurement of thermo-optic properties of Y<sub>3</sub>Al<sub>5</sub>O<sub>12</sub>, Lu<sub>3</sub>Al<sub>5</sub>O<sub>12</sub>, YAlO<sub>3</sub>, LiYF<sub>4</sub>, LiLuF<sub>4</sub>, BaY<sub>2</sub>F<sub>8</sub>, KGd(WO<sub>4</sub>)<sub>3</sub>, and KY(WO<sub>4</sub>)<sub>2</sub> laser crystals in the 80–300 K temperature range," *J. Appl. Phys.* **98**(10), 103514 (2005).
23. K. Yumashev and P. Loiko, "Thermal stresses and end-bulging in the laser disc from a tetragonal crystal: The case of LiYF<sub>4</sub>," *Laser Phys.* **25**(6), 065004 (2015).
24. F. Cornacchia, D. Parisi, C. Bernardini, A. Toncelli, and M. Tonelli, "Efficient, diode-pumped Tm<sup>(3+)</sup>:BaY<sub>2</sub>F<sub>8</sub> vibronic laser," *Opt. Express* **12**(9), 1982–1989 (2004).
25. P. Loiko, J. M. Serres, X. Mateos, K. Yumashev, N. Kuleshov, V. Petrov, U. Griebner, M. Aguiló, and F. Díaz, "Microchip laser operation of Tm:Ho:KLu(WO<sub>4</sub>)<sub>2</sub> crystal," *Opt. Express* **22**(23), 27976–27984 (2014).
26. X. Zhang, Y. Wang, L. Li, Y. Ju, and Y. Peng, "The effects of energy transfer upconversion on end-pumped Q-switched Tm:Ho:YLF lasers," *J. Phys. D Appl. Phys.* **42**(2), 025107 (2009).
27. P. Loiko, X. Mateos, S. Y. Choi, F. Rotermund, J. M. Serres, M. Aguiló, F. Díaz, K. Yumashev, U. Griebner, and V. Petrov, "Vibronic thulium laser at 2131 nm Q-switched by single-walled carbon nanotubes," *J. Opt. Soc. Am. B* **33**(11), D19–D27 (2016).
28. M. Dulick, G. E. Faulkner, N. J. Cockroft, and D. C. Nguyen, "Spectroscopy and dynamics of upconversion in Tm<sup>3+</sup>:YLiF<sub>4</sub>," *J. Lumin.* **48–49**, 517–521 (1991).
29. S. A. Miller, H. E. Rast, and H. H. Caspers, "Lattice vibrations of LiYF<sub>4</sub>," *J. Chem. Phys.* **52**(8), 4172–4175 (1970).
30. P. Loiko, F. Druon, P. Georges, B. Viana, and K. Yumashev, "Thermo-optic characterization of Yb:CaGdAlO<sub>4</sub> laser crystal," *Opt. Mater. Express* **4**(11), 2241–2249 (2014).
31. K. V. Yumashev, A. N. Zakharova, and P. A. Loiko, "Photo-elastic effect, thermal lensing and depolarization in  $\alpha$ -cut tetragonal laser crystals," *Laser Phys.* **26**(6), 065002 (2016).
32. P. A. Loiko, K. V. Yumashev, V. N. Matrosov, and N. V. Kuleshov, "Dispersion and anisotropy of thermo-optic coefficients in tetragonal GdVO<sub>4</sub> and YVO<sub>4</sub> laser host crystals," *Appl. Opt.* **52**(4), 698–705 (2013).
33. K. van Dalen, S. Aravazhi, C. Grivas, S. M. García-Blanco, and M. Pollnau, "Thulium channel waveguide laser with 1.6 W of output power and ~80% slope efficiency," *Opt. Lett.* **39**(15), 4380–4383 (2014).
34. J. A. Caird, S. A. Payne, P. R. Staber, A. J. Ramponi, L. L. Chase, and W. F. Krupke, "Quantum electronic properties of the Na<sub>3</sub>Ga<sub>2</sub>Li<sub>3</sub>F<sub>12</sub>:Cr<sup>3+</sup> laser," *IEEE J. Quantum Electron.* **24**(6), 1077–1099 (1988).
35. T. Yokozawa, J. Izawa, and H. Hara, "Mode control of a Tm:YLF microchip laser by a multiple resonator," *Opt. Commun.* **145**(1–6), 98–100 (1998).
36. G. L. Bourdet and G. Lescroart, "Theoretical modeling and design of a Tm, Ho:YLiF<sub>4</sub> microchip laser," *Appl. Opt.* **38**(15), 3275–3281 (1999).
37. F. Druon, S. Ricaud, D. N. Papadopoulos, A. Pellegrina, P. Camy, J. L. Doualan, R. Moncorgé, A. Courjaud, E. Mottay, and P. Georges, "On Yb:CaF<sub>2</sub> and Yb:SrF<sub>2</sub>: review of spectroscopic and thermal properties and their impact on femtosecond and high power laser performance," *Opt. Mater. Express* **1**(3), 489–502 (2011).

## 1. Introduction

The tetragonal lithium yttrium fluoride, LiYF<sub>4</sub> (shortly YLF), is a well-known crystalline laser host for trivalent lanthanide ions. Nowadays, it is widely used in efficient and power-

scalable continuous-wave (CW) and passively Q-switched (PQS) lasers emitting at  $\sim 1 \mu\text{m}$  (Nd:YLF) and  $\sim 1.9 \mu\text{m}$  (Tm:YLF) [1,2]. The Tm:YLF lasers based on the  ${}^3\text{F}_4 \rightarrow {}^3\text{H}_6$  transition of the  $\text{Tm}^{3+}$  ion are used in laser surgery and for pumping of high-power or high-energy Ho-doped oscillators [3]. Tm:YLF has several advantages. First, the host matrix, YLF, possesses relatively high thermal conductivity,  $\sim 6 \text{ W/(m}\cdot\text{K)}$  [4] which is of high relevance for power scaling. Second, from the spectroscopic point of view, it permits relatively high Tm doping levels (3–8 at.% or  $N_{\text{Tm}} = 4\text{--}11 \times 10^{20} \text{ cm}^{-3}$ ) providing efficient cross-relaxation (CR) for the adjacent  $\text{Tm}^{3+}$  ions ( ${}^3\text{H}_4(\text{Tm}_1) + {}^3\text{H}_6(\text{Tm}_2) \rightarrow {}^3\text{F}_4(\text{Tm}_1) + {}^3\text{F}_4(\text{Tm}_2)$ ) [1] leading to a quantum efficiency of  $\sim 2$  and, consequently, to high laser efficiency. It is characterized by a very long  $\text{Tm}^{3+}$  upper-laser-level lifetime ( $\sim 16 \text{ ms}$ ) [5] leading to low laser threshold in CW and to high pulse energies achievable in the PQS regime, e.g. 0.9 mJ were generated in [6] with a pulse duration of 14 ns at  $\sim 1.9 \mu\text{m}$  using a  $\text{Cr}^{2+}$ :ZnS saturable absorber (SA). Third, Tm:YLF exhibits natural birefringence and anisotropy of the transition cross-sections [5] which eliminates the depolarization loss and provides a natural selection of the linear laser polarization. Fourth, YLF like most of the fluorides exhibits negative thermo-optic coefficient,  $dn/dT$ , which leads to weak thermal lens for certain crystal orientations [4,7]. Finally, Tm:YLF can be efficiently pumped by commercial AlGaAs laser diodes emitting at  $\sim 791 \text{ nm}$  (into the  ${}^3\text{H}_6 \rightarrow {}^3\text{H}_4$  band of  $\text{Tm}^{3+}$ ) [1].

There exist two other fluorides isostructural to YLF. These are  $\text{LiGdF}_4$  and  $\text{LiLuF}_4$  (shortly GLF and LLF, respectively) [8,9] which have attracted a lot of attention in recent years for the design of PQS Tm lasers. Again due to the long storage time of the  ${}^3\text{F}_4$  upper laser level, these crystals generated 0.47 mJ/13 ns (Tm:GLF) and 1.26 mJ/7.6 ns (Tm:LLF) pulses at  $\sim 1.9 \mu\text{m}$ , with  $\text{Cr}^{2+}$ :ZnS and  $\text{Cr}^{2+}$ :ZnSe SAs, respectively [10,11]. Such laser sources are of practical importance for medicine and sensing of  $\text{CO}_2$  and water in the atmosphere.

The microchip laser concept implies the gain material and (optionally) a SA placed in a compact low-loss plano-plano cavity [12,13]. As for Tm lasers, and, in particular, Tm:YLF, it is known that the upconversion mechanism is a key factor limiting the laser performance for high doping levels [1]. The application of the microchip concept can partially mitigate this drawback by keeping low intracavity losses and, hence, a low inversion level in the active medium, thus fully exploiting the advantages of highly Tm-doped crystals (high pump and CR efficiencies) leading to high laser efficiency [14]. For PQS lasers, the microchip concept offers short output pulses due to the reduction of the cavity roundtrip time [13]. Indeed, the shortest (few ns-long or even sub-ns) pulses from a PQS oscillator at  $\sim 2 \mu\text{m}$  were reported in PQS Tm microchip lasers [15,16]. An important remark about microchip lasers is that they require a positive thermal lens of the active material to ensure the stabilization of the laser mode [14].

In the present work, we report on a detailed comparative investigation of the three tetragonal  $\text{Tm:LiLnF}_4$  crystals (with  $\text{Ln} = \text{Y, Gd, and Lu}$ ) for microchip lasers at  $\sim 1.91 \mu\text{m}$  and even beyond  $\sim 2 \mu\text{m}$ , including a comparison of their spectroscopic properties, parameters of the thermal lens and the laser performance.

## 2. Experimental

### 2.1 Studied crystals

The three  $\text{LiLnF}_4$  crystals (with  $\text{Ln} = \text{Y, Gd, and Lu}$ ) studied were grown by the Czochralski method using  $\text{LiF}$ ,  $\text{LnF}_3$  and  $\text{TmF}_3$  (and  $\text{HoF}_3$ ) reagents. The YLF and GLF crystals were doped with 8 at.%  $\text{Tm}^{3+}$ , and the LLF crystals - with 8 and 12 at.%  $\text{Tm}^{3+}$ . High doping levels are selected to provide efficient CR for  $\text{Tm}^{3+}$  ions and increase the pump absorption. In addition, one codoped 5.2 at.%  $\text{Tm}^{3+}$ , 0.5 at.%  $\text{Ho}^{3+}$ :YLF crystal was studied.

The  $\text{Tm:LiLnF}_4$  crystals are tetragonal (space group  $\text{C}_{4h}^{64} - \text{I}_4/\text{a}$ ). For YLF, the lattice parameters are  $a = b = 5.164 \text{ \AA}$ ,  $c = 10.741 \text{ \AA}$ . The as-grown bulks were oriented with the X-ray Laue technique. All laser elements were cut for light propagation along the  $a$ -axis and polished to laser quality. They remained uncoated. Their dimensions as well as the Tm content are listed in Table 1. The  $\text{Tm:LiLnF}_4$  crystals are optically uniaxial with the optical

axis parallel to the  $c$ -axis. Thus, for an  $a$ -cut crystal, two principal light polarizations are available,  $E \parallel c$  ( $\pi$ ) and  $E \perp c$  ( $\sigma$ ). The refractive indices of YLF at  $\sim 1.91 \mu\text{m}$  are  $n_o = 1.443$  and  $n_e = 1.465$  (positive uniaxial).

Table 1. Parameters of the Studied Tm:LiLnF<sub>4</sub> Crystals

| Crystal                      | $N_{\text{RE}}, 10^{20} \text{ cm}^{-3}$ | $t, \text{ mm}$ | Aperture, $\text{mm}^2$ | Abs, %* |
|------------------------------|--|-----------------|-------------------------|---------|
| 8.0 at.% Tm:YLF              | 11.1                                     | 3.38            | $3.10(c) \times 2.96$   | 58      |
| 8.0 at.% Tm:GLF              | 10.6                                     | 2.70            | $3.11(c) \times 3.40$   | 45      |
| 8.0 at.% Tm:LLF              | 11.5                                     | 2.63            | $3.17(c) \times 3.22$   | 46      |
| 12.0 at.% Tm:LLF             | 17.2                                     | 3.54            | $3.15(c) \times 2.75$   | 76      |
| 5.2 at.% Tm, 0.5 at.% Ho:YLF | 7.2 (Tm), 0.7 (Ho)                       | 3.68            | $3.07(c) \times 2.63$   | 49      |

\*Total pump absorption in a micro-laser diode-pumped at  $\sim 791 \text{ nm}$ , defined as  $\text{Abs} = P_{\text{abs}}/P_{\text{inc}}$ .

## 2.2 Microchip-type set-up

The laser crystals were placed in a plano-plano laser cavity, Fig. 1(a). They were wrapped in indium foil and mounted in a Cu-holder water-cooled to  $12^\circ\text{C}$ . The cooling was provided from all 4 lateral sides. The pump mirror (PM) was anti-reflection (AR)-coated for  $0.78\text{--}1.0 \mu\text{m}$  and high-reflection (HR)-coated for  $1.8\text{--}2.1 \mu\text{m}$ . A set of output couplers (OCs) with transmission  $T_{\text{OC}} = 0.2\%$ ,  $0.5\%$ ,  $3\%$ ,  $5\%$  and  $10\%$  in the  $1.8\text{--}2.1 \mu\text{m}$  spectral range were used. Both mirrors were placed as close as possible to the laser crystal. The geometrical cavity length was equal to the crystal thickness, cf. Table 1. The crystal was pumped using a fiber-coupled (numerical aperture  $\text{NA} = 0.15$ , fiber core diameter:  $105 \mu\text{m}$ ) AlGaAs laser diode (diode #1) temperature-tuned to  $\lambda_p \sim 791 \text{ nm}$  ( $^3\text{H}_6 \rightarrow ^3\text{H}_4$  transition of the  $\text{Tm}^{3+}$  ion, Fig. 1(b)). The pump radiation was unpolarized. The output from the diode was collimated and focused into the crystal through the PM with a lens assembly (1:1 reimaging ratio,  $30 \text{ mm}$  focal length). The radius of the pump beam was  $w_p = 50 \mu\text{m}$  and its Rayleigh length  $2z_R = 1.0 \text{ mm}$  ( $M^2 \sim 31$  for the pump beam). The OCs were partially reflecting at  $\lambda_p$  ( $\sim 45\%$ ), so the pumping was in two passes. The total pump absorption under lasing conditions is specified in Table 1.

Strictly speaking, a *monolithic* microchip laser requires that both dielectric cavity mirrors are directly deposited onto the surfaces of the active element (or a stack of the active element and a SA) [12]. In our case, we may talk about a microchip-type laser or a micro-laser that is a prerequisite for the further design of monolithic devices.

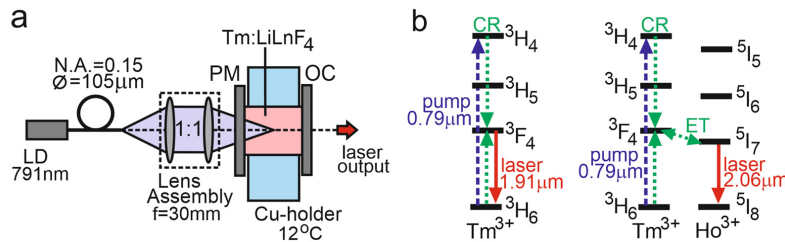


Fig. 1. (a) Scheme of the Tm:LiLnF<sub>4</sub> micro-lasers: LD – laser diode, PM – pump mirror, OC – output coupler; (b) Scheme of the energy-levels of  $\text{Tm}^{3+}$  and  $\text{Ho}^{3+}$  ions showing the pump and laser transitions: CR – cross-relaxation, ET – energy-transfer.

## 2.3 Thermal lens measurements

The thermal lens was measured in the 8 at.% Tm:YLF, the 8 at.% Tm:GLF and the 12 at.% Tm:LLF crystals by analyzing the divergence of the output laser beam at various absorbed pump powers  $P_{\text{abs}}$ , see [17] for more details. A hemispherical laser cavity (radius of the OC:  $R_{\text{OC}} = 50 \text{ mm}$ ,  $T_{\text{OC}} = 5\%$ , cavity length:  $49 \text{ mm}$ ) was used. The crystal was pumped by a fiber-coupled ( $\text{N.A.} = 0.22$ , fiber core diameter:  $200 \mu\text{m}$ ) AlGaAs laser diode (diode #2) emitting unpolarized radiation at  $\lambda_p = 802 \text{ nm}$  ( $2z_R = 1.9 \text{ mm}$ ,  $M^2 \sim 59$ ). The choice of this diode #2 is explained by better mode-matching of the pump ( $w_p = 100 \mu\text{m}$ ) and laser ( $w_L = 95 \pm 15 \mu\text{m}$ , depending on the thermal lens) beams in the crystal resulting in lower  $M^2$  parameter of the output beam that is desirable for thermal lens evaluation.

The optical (refractive) power of the thermal lens  $D$  (inverse of the focal length,  $D = 1/f$ ) was calculated within the ray transfer matrix formalism [18]. The thermal lens was considered as an ideal thin astigmatic lens located at the center of the crystal. The radius of the output laser beam was measured by the optical knife method in the directions parallel and perpendicular to the laser polarization  $E$ . For each measurement, the  $M^2$  parameter of the laser beam was taken into account; it was in the 1.1-2 range for the studied  $P_{\text{abs}}$  (as measured in accordance with the ISO 11146-1 standard).

### 3. Spectroscopic properties

At first, we compared the transition cross-sections of the  $\text{Tm}^{3+}$  ions in the  $\text{LiLnF}_4$  crystals relevant for diode-pumped microchip laser operation. The  $\text{Tm}^{3+}$  ions in the  $\text{LiLnF}_4$  structure replace the “passive”  $\text{Ln}^{3+}$  ions in only one site ( $S_4$  symmetry) with VIII-fold  $O^{2-}$ -coordination. The absorption cross-sections,  $\sigma_{\text{abs}}$ , for the  ${}^3\text{H}_6 \rightarrow {}^3\text{H}_4$  and  ${}^3\text{H}_6 \rightarrow {}^3\text{F}_4$  transitions of  $\text{Tm}^{3+}$  ions in a 8 at.% Tm:YLF crystal are shown in Fig. 2(a). They have been determined as  $\sigma_{\text{abs}} = \alpha_{\text{abs}}/N_{\text{Tm}}$  where  $\alpha_{\text{abs}}$  is the absorption coefficient; the absorption spectra were measured in polarized light ( $E \parallel c$  and  $E \perp c$ ) for  $a$ -cut polished crystals. For the  ${}^3\text{H}_6 \rightarrow {}^3\text{H}_4$  transition,  $\sigma_{\text{abs}}$  is higher for  $E \parallel c$  (the maximum value is  $0.79 \times 10^{-20} \text{ cm}^2$  at 780.2 nm, the full width at half maximum, FWHM, of this peak is 7.7 nm). For  $E \perp c$ , the maximum  $\sigma_{\text{abs}}$  is  $0.36 \times 10^{-20} \text{ cm}^2$  at 790.6 nm, and FWHM = 16.4 nm. For the  ${}^3\text{H}_6 \rightarrow {}^3\text{F}_4$  transition, the maximum  $\sigma_{\text{abs}} = 1.21 \times 10^{-20} \text{ cm}^2$  is observed at 1681.6 nm for  $E \parallel c$ . The absorption properties of the Tm:YLF, Tm:GLF and Tm:LLF crystals are similar, see Fig. 2(b,c). Note the red-shift of the absorption of  $\text{Tm}^{3+}$  ions in GLF due to the larger difference of ionic radii of  $\text{Tm}^{3+}$  (0.994 Å) and  $\text{Gd}^{3+}$  (1.053 Å) as compared with  $\text{Y}^{3+}$  and  $\text{Lu}^{3+}$ .

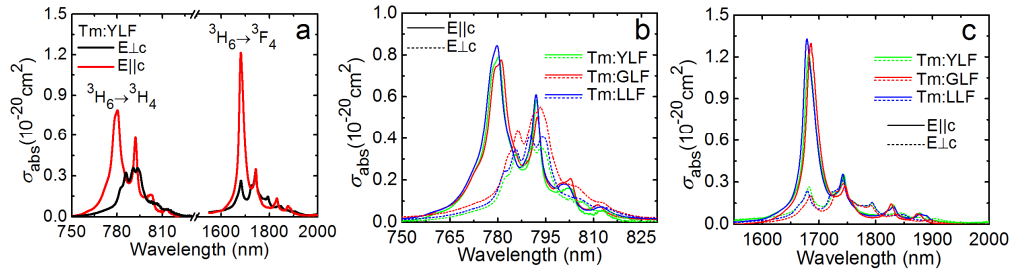


Fig. 2. Absorption cross-section,  $\sigma_{\text{abs}}$ , spectra for the  ${}^3\text{H}_6 \rightarrow {}^3\text{H}_4$  and  ${}^3\text{H}_6 \rightarrow {}^3\text{F}_4$  transitions of  $\text{Tm}^{3+}$  in 8 at.% Tm-doped YLF, GLF and LLF crystals for light polarizations  $E \perp c$  and  $E \parallel c$ : (a) Tm:YLF crystal; (b) comparison for the  ${}^3\text{H}_6 \rightarrow {}^3\text{H}_4$  transition; (c) comparison for the  ${}^3\text{H}_6 \rightarrow {}^3\text{F}_4$  transition.

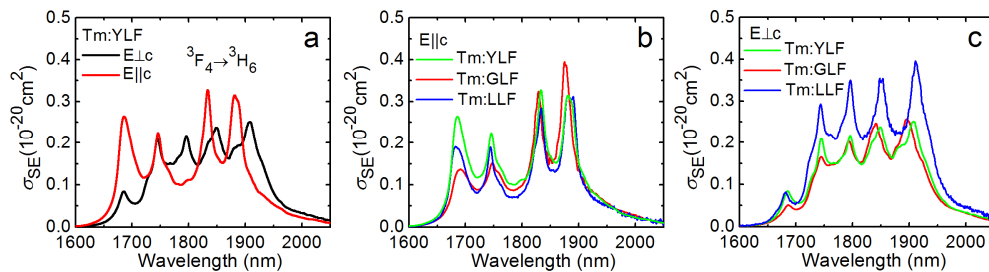


Fig. 3. Stimulated-emission (SE) cross-section,  $\sigma_{\text{SE}}$ , spectra for the  ${}^3\text{F}_4 \rightarrow {}^3\text{H}_6$  transition of  $\text{Tm}^{3+}$  in 8 at.% Tm-doped YLF, GLF and LLF crystals for light polarizations  $E \perp c$  and  $E \parallel c$ : (a) Tm:YLF crystal; (b) comparison for  $E \parallel c$  polarization; (c) comparison for  $E \perp c$  polarization.

The stimulated-emission (SE) cross-sections,  $\sigma_{\text{SE}}$ , for the  ${}^3\text{F}_4 \rightarrow {}^3\text{H}_6$  transition of  $\text{Tm}^{3+}$ , see Fig. 1(b), derived by a combination of the reciprocity and Füchtbauer–Ladensburg (F-L)



methods [19,20], are shown in Fig. 3. For  $\text{Tm}^{3+}$  in YLF, the maximum  $\sigma_{\text{SE}}$  corresponds to  $\mathbf{E} \parallel \mathbf{c}$ ,  $0.33 \times 10^{-20} \text{ cm}^2$  at 1833.4 nm and it is lower for  $\mathbf{E} \perp \mathbf{c}$ ,  $0.25 \times 10^{-20} \text{ cm}^2$  at 1907.7 nm, see Fig. 3(a).  $\text{Tm}^{3+}$  represents a quasi-three-level laser scheme [21]. In the spectral range where lasing occurs (long-wavelength part of the emission band), the  $\sigma_{\text{SE}}$  are higher for  $\mathbf{E} \perp \mathbf{c}$  than for  $\mathbf{E} \parallel \mathbf{c}$  for all the  $\text{Tm}:\text{LiLnF}_4$  crystals. The corresponding local peak in the SE cross-section spectra is located at  $\sim 1908$  nm for  $\text{Tm}:\text{YLF}$ , 1900 nm for  $\text{Tm}:\text{GLF}$  and 1912 nm for  $\text{Tm}:\text{LLF}$ , see Fig. 3(c). A summary of the spectroscopic characteristics of the  $\text{Tm}:\text{LiLnF}_4$  crystals is presented in Table 2.

Table 2. Comparison of the Spectroscopic Characteristics of the  $\text{Tm}:\text{LiLnF}_4$  Crystals

| Crystal | $\sigma_{\text{abs}}, 10^{-20} \text{ cm}^2$ |  |                                   |  | $\sigma_{\text{SE}}, 10^{-20} \text{ cm}^2$ |                                   |                                   |                                   |
|---------|--|--|-----------------------------------|--|---|-----------------------------------|-----------------------------------|-----------------------------------|
|         | $\mathbf{E} \perp \mathbf{c}$                | $\lambda_{\text{abs}} (\Delta\lambda), \text{ nm}$ | $\mathbf{E} \parallel \mathbf{c}$ | $\lambda_{\text{abs}} (\Delta\lambda), \text{ nm}$ | $\mathbf{E} \perp \mathbf{c}$               | $\lambda_{\text{em}}, \text{ nm}$ | $\mathbf{E} \parallel \mathbf{c}$ | $\lambda_{\text{em}}, \text{ nm}$ |
| Tm:LLF  | 0.41   | 790.2 (16.8)                                       | 0.84                              | 779.8 (7.7)  | 0.39  | 1912                              | 0.31                              | 1881                              |
| Tm:YLF  | 0.36   | 790.6 (16.4)                                       | 0.79                              | 780.2 (7.7)  | 0.25  | 1908                              | 0.31                              | 1881                              |
| Tm:GLF  | 0.55   | 793.5 (15.5)                                       | 0.77                              | 781.1 (8.3)  | 0.26  | 1900                              | 0.39                              | 1875                              |

\* $\lambda_{\text{abs}}$  and  $\lambda_{\text{em}}$  – peak absorption and emission wavelengths, respectively;  $\Delta\lambda$  – FWHM of the absorption peak.

The selection of an  $\mathbf{a}$ -cut or  $\mathbf{c}$ -cut  $\text{Tm}:\text{LiLnF}_4$  crystal for microchip operation is based on both the spectroscopic and thermo-optic properties. According to the  $\sigma_{\text{abs}}$  spectra for the  $^3\text{H}_6 \rightarrow ^3\text{H}_4$  transition,  $\mathbf{a}$ -cut  $\text{Tm}:\text{LiLnF}_4$  crystals are more attractive in terms of higher pump efficiency. In addition, for this crystal cut, the anisotropy of the SE cross-sections of  $\text{Tm}^{3+}$  and the natural birefringence of the host promote the linearly polarized laser output.

Regarding the thermo-optic effects, the microchip lasers depend on the so-called thermal mode stabilization (thermal guiding) in a plano-plano laser cavity which is provided only by positive thermal lens. Characteristic of all these fluoride crystals and, in particular, of YLF is a negative thermo-optic coefficient,  $dn_o/dT = -4.6 \times 10^{-6} \text{ K}^{-1}$  and  $dn_e/dT = -6.6 \times 10^{-6} \text{ K}^{-1}$  [22]. Thus, positive thermal lens in this material is possible if only the negative contribution of  $dn/dT$  is cancelled by the positive contribution of the thermal expansion  $\alpha$ . This can be expressed by the so-called “generalized” thermo-optic coefficient:  $\Delta \approx dn/dT + (1 + \nu)(n - 1)\alpha$ , where  $\nu$  is the Poisson ratio ( $\nu = 0.33$  for YLF) [23]. Specifically for YLF,  $\alpha_a > \alpha_c$ , namely  $14.3 \times 10^{-6} \text{ K}^{-1}$  and  $10.1 \times 10^{-6} \text{ K}^{-1}$ , respectively [22]. Thus, it is desirable to work with  $\mathbf{a}$ -cut  $\text{Tm}:\text{LiLnF}_4$  crystals which will provide stronger positive thermal lens due to the above-mentioned compensation ( $\Delta \approx + 3.8 \times 10^{-6} \text{ K}^{-1}$ ). For an  $\mathbf{a}$ -cut  $\text{Tm}:\text{YLF}$  crystal, the polarization ( $\mathbf{E} \perp \mathbf{c}$ ) in the microchip laser will be selected also by the expected negative sign of the thermal lens for the  $\mathbf{E} \parallel \mathbf{c}$  polarization [4].

#### 4. $\text{Tm}:\text{LiLnF}_4$ micro-lasers

##### 4.1 Comparison of output performance

Laser operation in a plano-plano cavity was achieved with all four studied  $\text{Tm}:\text{LiLnF}_4$  crystals (cf. Table 1). In all cases, the laser output was linearly polarized,  $\mathbf{E} \perp \mathbf{c}$  ( $\sigma$ ).

The output characteristics for the 8 at.%  $\text{Tm}:\text{YLF}$  micro-laser are shown in Fig. 4(a). The best output performance corresponded to  $T_{\text{OC}} = 5\%$ . This laser generated 3.1 W at 1904 nm with a slope efficiency of  $\eta = 72\%$  (with respect to  $P_{\text{abs}}$ ). The laser threshold was at  $P_{\text{abs}} = 0.24$  W and the optical-to-optical efficiency reached  $\eta_{\text{opt}} = 38\%$  (with respect to the incident power). For  $T_{\text{OC}} = 10\%$ , the laser output was deteriorated which is attributed to increased upconversion losses related to higher inversion ratio  $\beta$  for  $\text{Tm}^{3+}$  ions. With the increase of  $T_{\text{OC}}$ , the laser emission wavelength shortened from 1991 to 2018 nm for  $T_{\text{OC}} = 0.2\%$  to 1900–1916 nm for  $T_{\text{OC}} = 10\%$ , see Fig. 4(b). This behavior is due to the quasi-three-level nature of the  $\text{Tm}^{3+}$  emission and it is in agreement with the gain cross-section,  $\sigma_g = \beta\sigma_{\text{SE}} - (1-\beta)\sigma_{\text{abs}}$ , spectra when increasing the inversion ratio  $\beta$ , Fig. 4(c). The multi-peak spectral behavior is explained by the etalon effects resulting from the small separations of the optical elements in the microchip-type cavity. This effect is potentially interesting for THz generation. The emission at  $\sim 2 \mu\text{m}$  observed for low  $T_{\text{OC}}$  is due to the electron-phonon coupling (vibronic

laser emission) [24]. The generation of  $\sigma$ -polarized output is in agreement with the dominance of  $\sigma_g(E \perp c)$  over  $\sigma_g(E \parallel c)$  at low inversion ratios,  $\beta < 0.3$ , Fig. 4(c), although the relation of the peak SE cross-sections is opposite, see Fig. 3(a).

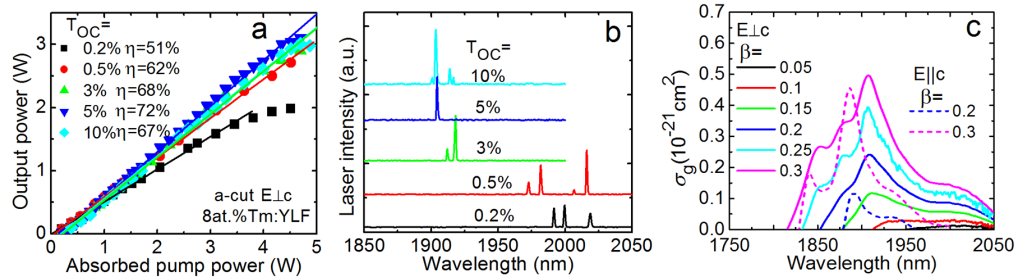


Fig. 4. Tm:YLF micro-laser: (a) input-output dependences,  $\eta$  – slope efficiency; (b) typical laser emission spectra at  $P_{\text{abs}} = 4.5$  W; (c) gain cross-section,  $\sigma_g = \beta\sigma_{\text{SE}} - (1 - \beta)\sigma_{\text{abs}}$ , spectra for Tm:YLF for light polarizations  $E \perp c$  ( $\sigma$ ) and  $E \parallel c$  ( $\pi$ ),  $\beta$  is the inversion ratio.

In Fig. 5(a), we compared the laser performance of all four studied Tm-doped crystals (Table 1) for the same  $T_{\text{OC}} = 5\%$ . The Tm:GLF laser generated 1.87 W at 1902 nm with  $\eta = 65\%$  and  $\eta_{\text{opt}} = 27\%$ . The laser threshold was at  $P_{\text{abs}} = 0.29$  W. The power scaling was limited by lower absorption and lower thermal fracture limit which is most probably due to a higher lattice distortion owing to the difference in ionic radii of  $\text{Tm}^{3+}$  and  $\text{Gd}^{3+}$ . The Tm:LLF laser with the 12 at.% Tm-doped crystal generated 2.65 W at 1916 nm with  $\eta = 52\%$  and  $\eta_{\text{opt}} = 37\%$ . The laser threshold was at  $P_{\text{abs}} = 0.46$  W. For the LLF crystal with 8 at.% Tm doping, the output performance was inferior. For the same 5% OC, the emission wavelength shortened following the Tm:LLF – Tm:YLF – Tm:GLF series, Fig. 5(c), in agreement with the position of the long-wavelength local peak in the  $\sigma_{\text{SE}}$  spectra, as shown in Fig. 3(c). A summary of the output characteristics of the Tm:LiLnF<sub>4</sub> micro-lasers is presented in Table 3.

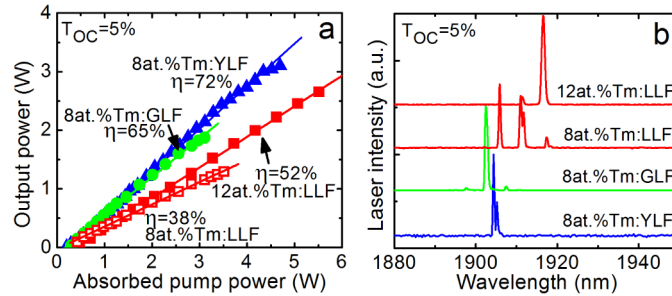


Fig. 5. Comparison of the (a) input-output characteristics and (b) typical laser emission spectra (at maximum  $P_{\text{abs}}$ ) for Tm:YLF, Tm:GLF and Tm:LLF micro-lasers,  $\eta$  – slope efficiency.

Table 3. Comparison of the Output Characteristics of the Tm:LiLnF<sub>4</sub> Micro-Lasers

| Crystal          | $P_{\text{out}}$ , W | $\lambda_{\text{L}}$ , nm | $\eta$ , % | $P_{\text{th}}$ , W | $\eta_{\text{opt}}$ , % |
|------------------|----------------------|---------------------------|------------|---------------------|-------------------------|
| 12.0 at.% Tm:LLF | 2.65                 | 1916                      | 52         | 0.46                | 37                      |
| 8.0 at.% Tm:YLF  | 3.10                 | 1904                      | 72         | 0.24                | 38                      |
| 8.0 at.% Tm:GLF  | 1.87                 | 1902                      | 65         | 0.29                | 27                      |

#### 4.2 Micro-lasers beyond 2 $\mu\text{m}$

Laser operation beyond 2  $\mu\text{m}$  with Tm-doped crystals is possible in two ways. One approach is the codoping with  $\text{Ho}^{3+}$  ions (keeping the Ho/Tm ratio low to minimize the upconversion mechanism) [25]. The  $\text{Ho}^{3+}$  ion emits above 2  $\mu\text{m}$  according to the  $^5\text{I}_7 \rightarrow ^5\text{I}_8$  transition, and the excitation is provided by the energy-transfer (ET)  $\text{Tm}^{3+}(^3\text{F}_4) \rightarrow \text{Ho}^{3+}(^5\text{I}_7)$ , see Fig. 1(b). The results for the 5.2 at.% Tm, 0.5 at.% Ho:YLF crystal are shown in Fig. 6(a). The maximum output power from this laser reached 378 mW at 2065 nm corresponding to  $\eta =$

25% ( $T_{OC} = 3\%$ ). The laser threshold was at  $P_{abs} = 0.48$  W and  $\eta_{opt} = 9\%$ . The laser operated with  $\mathbf{E} \perp \mathbf{c}$  polarization and the emission wavelength was weakly dependent on the OC, see Fig. 6(b), corresponding to a local maximum in the  $\sigma_{SE}$  spectra of the  $\text{Ho}^{3+}$  ions in YLF, Fig. 6(c). A thermal roll-over was observed for  $P_{abs} > 2$  W attributed to a much stronger heating of the crystal related to upconversion [25,26] and finite ET probability. Indeed, the fractional heat loading,  $\eta_h \approx 0.45$  for Tm,Ho:YLF [26].

The second approach to achieve laser operation with a  $\text{Tm}^{3+}$ -doped crystal beyond 2  $\mu\text{m}$  is the so-called vibronic coupling [24,27]. For  $\text{Tm}^{3+}$  in YLF, the longest wavelength of the purely electronic  $^3F_4 \rightarrow ^3H_6$  transition is 1931 nm (it occurs between the lowest Stark sub-level of the  $^3F_4$  excite-state,  $5599\text{ cm}^{-1}$ , and the highest sub-level of the  $^3H_6$  ground-state,  $419\text{ cm}^{-1}$ ) [28]. Longer emission wavelengths are attributed to a coupling of the electrons that participate in the electronic transition  $^3F_4 \rightarrow ^3H_6$  with various phonons of the host (electron-phonon or vibronic coupling). The relaxation of a  $\text{Tm}^{3+}$  ion excited to the  $^3F_4$  state may lead to the excitation of a phonon and the emission of one photon with lower energy (longer wavelength) [27]. In Fig. 4(b), the emission at around 2  $\mu\text{m}$  observed for low  $T_{OC}$  (0.2, 0.5%) has a vibronic nature and it is supported by very smooth and broad gain spectra for low inversion ratios  $\beta < 0.05$  inherent to low outcoupling losses, Fig. 4(c).

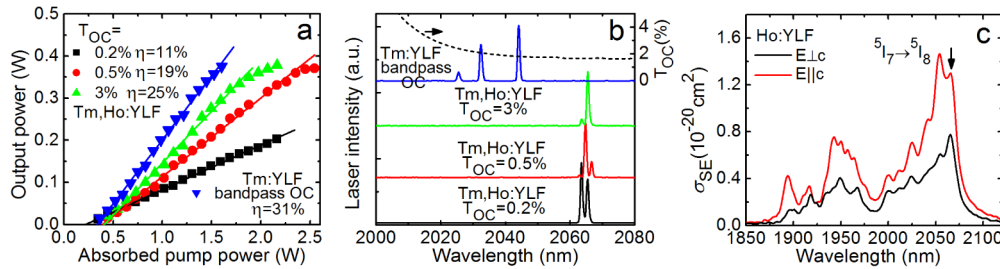


Fig. 6. (a) Input-output characteristics and (b) typical laser emission spectra (at maximum  $P_{abs}$ ) for the “vibronic” Tm:YLF micro-laser with a “bandpass” OC and the Tm,Ho:YLF micro-laser with different OCs,  $\eta$  - slope efficiency; dashed curve – transmission spectrum of the “bandpass” OC; (c)  $\sigma_{SE}$  spectra for the  $^5I_7 \rightarrow ^5I_8$  transition of  $\text{Ho}^{3+}$  in YLF for light polarizations  $\mathbf{E} \perp \mathbf{c}$  ( $\sigma$ ) and  $\mathbf{E} \parallel \mathbf{c}$  ( $\pi$ ), arrow denotes the laser wavelength.

The vibronic operation at even longer wavelengths can be promoted by using a selective (“bandpass”) OC [27], e.g. as in the present work. Such OC was specified for high transmission at 1.9–1.97  $\mu\text{m}$  and  $T_{OC} = 1.6\%$  at 2.05–2.20  $\mu\text{m}$  (see the transmission spectrum in Fig. 6(a)). The results are shown in Fig. 6(a,b). The maximum output power reached 375 mW at 2026–2044 nm corresponding to  $\eta = 31\%$  (i.e., better than the Tm,Ho:YLF micro-laser). The laser threshold was  $P_{abs} = 0.35$  W and  $\eta_{opt} = 14\%$ . The maximum phonon energy of YLF  $\nu_{ph}$  is  $\sim 560\text{ cm}^{-1}$  [29]. The observed emission lines are attributed to the coupling with the Raman-active modes occurring at  $\nu_{ph} = 240\text{--}290\text{ cm}^{-1}$  and assigned as  $A_{g(u)}$  and  $B_g$  [29].

## 5. Thermal lensing

The thermal lensing in  $\text{LiLnF}_4$  crystals has been extensively studied for the case of diode-pumped Nd:YLF laser rods [4,7]. It was shown that the thermal lens is positive for an  $\mathbf{a}$ -cut crystal and  $\mathbf{E} \perp \mathbf{c}$  polarization. For Tm-doped YLF, only the information on the fractional heat load exists ( $\eta_h \approx 0.36$ ) [1]. Thermal stress and end-bulging in Tm:YLF crystals were evaluated theoretically in [23]. In the present work, we characterize, for the first time, the thermal lens in diode-pumped  $\mathbf{a}$ -cut Tm:YLF, Tm:GLF and Tm:LLF crystals.

The results on the optical power of the thermal lens are shown in Fig. 7 and summarized in Table 4. These results correspond to the polarization and wavelength of the built lasers. For all studied crystals, the polarization was  $\mathbf{E} \perp \mathbf{c}$  ( $\sigma$ ) and the emission spectra were similar to those plotted in Fig. 5(b). The thermal lens is positive (focusing) for all Tm: $\text{LiLnF}_4$  crystals. This finding is in agreement with the feasibility of microchip operation with these crystals,



Fig. 5(a). The thermal lens shows an almost linear dependence of its optical power on  $P_{\text{abs}}$ , expressed by the so-called sensitivity factor,  $M = dD/dP_{\text{abs}}$  [30]. The thermal lens in Tm:LiLnF<sub>4</sub> is astigmatic, as its optical power is different for rays lying in different meridional planes and is confirmed by the ellipticity of the output laser beam. The principal meridional planes of the thermal lens A(B) correspond to the beam semi-axes and in our case they coincide with the directions along the *a*- and *c*-axes. This agrees with the theoretical modeling and is related to the anisotropy of the thermal expansion [23].

The thermal lens is weaker for Tm:YLF than for the other two fluoride crystals,  $M = 4.0$  and  $3.6 \text{ m}^{-1}/\text{W}$  (for the meridional planes containing the directions  $\parallel c$  and  $\perp c$ -axis, respectively). For Tm:LLF, it is slightly stronger,  $M = 4.3$  ( $\parallel c$ ) and  $3.9$  ( $\perp c$ )  $\text{m}^{-1}/\text{W}$  and for Tm:GLF,  $M = 5.6$  ( $\parallel c$ ) and  $4.2$  ( $\perp c$ )  $\text{m}^{-1}/\text{W}$  for the two principal meridional planes, respectively. The astigmatism of the thermal lens is defined as the difference of its refraction in the principal meridional planes [30]. The astigmatism degree,  $S/M = |M_A - M_B|/M_{\text{max}}$  [30], equals 10%, 25% and 9% for Tm:YLF, Tm:GLF and Tm:LLF, respectively. Such a different thermo-optic behavior (stronger thermal lens with higher astigmatism) of the Tm:GLF crystal is attributed to a stronger distortion of its lattice with the incorporation of the Tm<sup>3+</sup> ions. The thermal lens astigmatism in *a*-cut tetragonal crystals is related to the net action of two effects: the photo-elastic effect and the stress-related component of end-bulging, both originating from the thermal stress in the crystal [31].

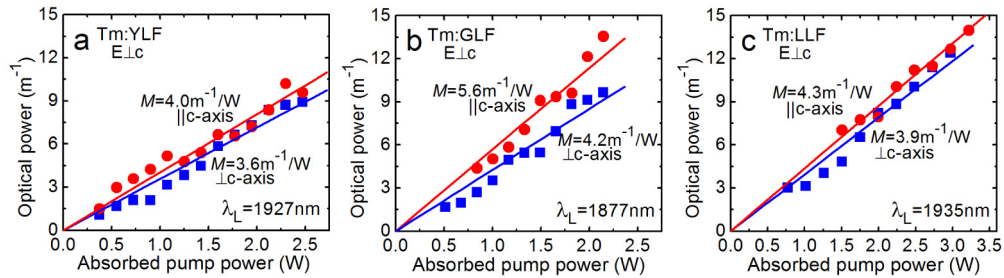


Fig. 7. Optical (refractive) power of the thermal lens vs. absorbed pump power in 8 at.% Tm:YLF (a), 8 at.% Tm:GLF (b) and 12 at.% Tm:LLF (c) crystals: pump wavelength,  $\lambda_p = 802 \text{ nm}$ ; pump spot radius,  $w_p = 100 \mu\text{m}$ , laser polarization,  $E \perp c$  ( $\sigma$ ): symbols – experimental data, lines – linear fits for the extraction of the sensitivity factor ( $M$ ).

Table 4. Comparison of the Thermal Lens Parameters of the Tm:LiLnF<sub>4</sub> Crystals (*a*-cut,  $E \perp c$ )

| Crystal          | $M, \text{m}^{-1}/\text{W}$ |           | $S/M, \%$ | $\lambda_L, \text{nm}$ |
|------------------|-----------------------------|-----------|-----------|------------------------|
|                  | $\parallel c$               | $\perp c$ |           |                        |
| 12.0 at.% Tm:LLF | 4.3                         | 3.9       | 9         | 1935                   |
| 8.0 at.% Tm:YLF  | 4.0                         | 3.6       | 10        | 1927                   |
| 8.0 at.% Tm:GLF  | 5.6                         | 4.2       | 25        | 1877                   |

The sensitivity factor of the thermal lens in a diode-pumped crystal is represented as [30]:

$$M = \frac{\eta_h}{2\pi w_p^2 \kappa} \cdot \Delta, \quad (1)$$

where  $\kappa$  is the thermal conductivity,  $5.3 \text{ W/mK}$  ( $\parallel c$ ) and  $7.2 \text{ W/mK}$  ( $\perp c$ ) for YLF [22]. In this formula, the pump beam is assumed to be “top-hat” [32]. Using the data for Tm:YLF, we calculate  $\Delta = 4.4$  and  $4.0 \times 10^{-6} \text{ K}^{-1}$  ( $\parallel c$  and  $\perp c$ , respectively) which agree with the value estimated above. The thermal lens in an *a*-cut Tm:YLF crystal is  $\sim 3$  times weaker than in an athermal *N<sub>g</sub>*-cut monoclinic Tm:KLu(WO<sub>4</sub>)<sub>2</sub> (Tm:KLuW) crystal previously studied under the same pump conditions ( $M = 12.9$  and  $8.1 \text{ m}^{-1}/\text{W}$  along the  $N_p$  and  $N_m$  axes, respectively, or, equivalently,  $\Delta = 8.8$  and  $5.5 \times 10^{-6} \text{ K}^{-1}$ , so  $S/M = 37\%$ ) [14]. The weaker thermal lens in

Tm:YLF is attributed to the higher thermal conductivity and lower  $\Delta$  in YLF due to the better compensation of the counteraction of  $dn/dT$  and  $\alpha$ . In addition, Tm:YLF provides lower astigmatism of the thermal lens.

It is worth noting that the thermal lens experiment was performed using the diode #2 ( $\lambda_p = 802$  nm,  $w_p = 100$   $\mu$ m) targeting a better precision of the evaluated optical power  $D$ , while in the microchip laser experiment – using the diode #1 ( $\lambda_p = 791$  nm,  $w_p = 50$   $\mu$ m) the target was to achieve a higher slope efficiency. This difference does not influence the sign of the thermal lens, the relation of  $M$ -factors for the two meridional planes and the astigmatism degree  $S/M$ . The absolute value of  $M$  will vary mostly due to the difference in  $w_p$ . This effect can be accounted with Eq. (1).

The nearly spherical thermal lens in Tm:YLF ( $S/M = 10\%$ ) is responsible for the generation of an almost circular output laser beam in the corresponding micro-laser with a measured  $M_{x,y}^2 < 1.05$  at the maximum studied  $P_{abs}$ .

The thermal stress is the reason for thermal fracture of the laser crystals. For diode-end-pumped crystals (plane stress approximation), the fracture occurs when the tangential (hoop) stress  $\sigma_\theta$  at the crystal periphery exceeds the tensile stress  $\sigma_{TS}$  ( $\sim 40$  MPa for YLF) [23]. By using the previously reported method for stress calculations in tetragonal crystals [23], we determined the “stress sensitivity factor”,  $M_\sigma = d\sigma_\theta/dP_{abs}$  as 4.4 MPa/W that corresponds to the maximum stress of  $\sim 22$  MPa in the Tm:YLF crystal (below  $\sigma_{TS}$ ). Indeed, no thermal fracture of Tm:YLF was observed but the power scaling was limited by the thermal roll-over at high  $P_{abs}$ , Fig. 4(a). Thus, we attribute this roll-over to the temperature-dependence of the spectroscopic and thermal parameters of the crystal which was strongly heated due to localized heat loading under tight focusing of the pump beam.

## 6. Discussion

The very high slope efficiency achieved with the Tm:YLF micro-laser ( $T_{OC} = 5\%$ ) is a consequence of the efficient CR for adjacent Tm<sup>3+</sup> ions under high doping (8 at.%), the good mode-matching conditions when pumping with a small pump spot size and relatively low losses in the laser crystal (including low upconversion loss for small  $T_{OC}$ ). The slope efficiency of a Tm laser can be represented as [33]:

$$\eta = \eta_{St} \cdot \eta_q \cdot \eta_{mode} \cdot \eta_{OC}, \quad (2)$$

where the four terms denote the Stokes, quantum, mode-matching and outcoupling efficiencies, respectively.  $\eta_{St}$  is defined as  $\lambda_p/\lambda_L$  ( $\lambda_L$  – laser wavelength) and equals in our case,  $\eta_{St} = 0.415$ . For 8 at.% Tm-doped YLF,  $\eta_q > 1.96$  [1] due to an efficient CR. The mode overlap in the considered laser can be calculated with the determined parameters of the thermal lens. One needs to take into account the dependence of the  $M$ -factor of the thermal lens on  $w_p$ , see Eq. (1), so  $M' = M \cdot (w_p/w_p')^2$  where  $M'$  is a sensitivity factor corresponding to a different pump spot size  $w_p'$ . Then, we obtain  $w_L = 62 \pm 5$   $\mu$ m with  $\eta_{mode} \approx 0.94$ . The  $\eta_{OC}$  is expressed as  $\ln[1-T_{OC}]/\ln[(1-T_{OC}) \cdot (1-L)]$  where  $L$  is the roundtrip passive loss that can be estimated from the Caird plot [34], i.e. plotting the inverse of the slope efficiency vs. the inverse of the output coupling,  $1/\eta = 1/\eta_0 + (L/\eta_0) \cdot (1/T_{OC})$ . From the data presented in Fig. 4(a) with the exception of the  $T_{OC} = 10\%$  OC where the upconversion effects are not negligible, we estimate the loss coefficient as  $\delta \sim 0.0011$  cm<sup>-1</sup> ( $L < 1 \times 10^{-3}$ ). As a result,  $\eta_{OC} > 0.99$ . Finally, the theoretical value for  $\eta$  is 75% in good agreement with the experimental value (72%).

The previous work on Tm:YLF microchip laser focused on single-longitudinal-mode (SLM) operation and thus power scaling was not targeted [35]. Microchip lasers based on Tm:GLF and Tm:LLF have never been reported previously. In the present study, we report on efficient multi-watt microchip operation with all three Tm:LiLnF<sub>4</sub> crystals. As compared with a previous report on a Tm:KLuW microchip laser [14], we achieved, with Tm:YLF, a similar output power ( $\sim 3$  W) and much higher slope efficiency (78% vs. 50.4%). There are multiple reports on Tm,Ho:YLF microchip lasers operating both in the SLM and multi-mode regimes,

see e.g [36]. The authors in [36], achieved  $\sim 1$  W with  $\eta = 54\%$  using a 6 at.% Tm, 0.4 at.% Ho:YLF crystal in a monolithic design. These results are better than those in the present work most probably due to the non-optimum Ho/Tm codoping ratio.

The vibronic laser operation with Tm:YLF extends recent findings in this field with other fluoride (Tm:BaY<sub>2</sub>F<sub>8</sub>) [24] and oxide (Tm:KLuW) [27] Raman-active crystals. Further improvement of the laser output and efficiency of vibronic Tm:LiLnF<sub>4</sub> lasers is expected by using high Tm doping levels (8-12 at.%) and proper laser mirrors. In this way, we expect laser emission at  $\sim 2.05$ - $2.1$   $\mu\text{m}$ .

Further power scaling of Tm:LiLnF<sub>4</sub> microchip lasers is possible by optimizing the doping level (in our case for 8 at.% Tm doping of YLF, a clear effect of upconversion loss was detected for  $T_{\text{OC}} = 10\%$ , see Fig. 4(a)) and the pump spot size. In this way the temperature and stress fields in the laser crystal will be compromised. Consequently, the slope efficiency of the Tm:GLF and Tm:LLF microchip lasers may be enhanced up to  $\sim 70\%$ .

The performed study of the thermal lens in tetragonal Tm:LiLnF<sub>4</sub> crystals indicates the compensation of various effects ( $dn/dT$ , end-bulging related to the thermal expansion and the photo-elastic effect) leading to a positive thermal lens, a situation not reached for cubic (higher symmetry) fluorides such as CaF<sub>2</sub> or SrF<sub>2</sub> [37]. A similar effect is expected for the monoclinic (lower symmetry) Tm:BaY<sub>2</sub>F<sub>8</sub> crystal [24] which has not been exploited for microchip lasers yet. Further work will focus also on direct measurements of the  $dn/dT$  coefficients for the LiLnF<sub>4</sub> crystals.

## 7. Conclusion

Tetragonal Tm:LiLnF<sub>4</sub> crystals are attractive for highly-efficient microchip lasers, diode-pumped at  $\sim 791$  nm and operating at  $\sim 1.91$   $\mu\text{m}$ , due to the combination of a high Tm doping level (and, hence, efficient CR), their spectroscopic properties and weak, positive and low-astigmatic thermal lensing (for *a*-cut crystals). The relatively high thermal conductivity and acceptable tensile stress allows for power scaling to multi-watt output using very compact (few mm-long) devices. In this way, an *a*-cut 8 at.% Tm:YLF micro-laser generated 3.1 W at 1904 nm with a slope efficiency of  $\eta = 72\%$  and a laser threshold as low as 0.24 W while  $\sim 2$  W output power was achieved with both Tm:GLF and Tm:LLF. The possibility to operate such laser oscillators beyond  $\sim 2$   $\mu\text{m}$  (2000-2044 nm) is demonstrated with a Tm:YLF crystal using the vibronic coupling and compared to the conventional Tm,Ho-codoping scheme. The extension of the microchip concept to other anisotropic fluorides (Tm:BaY<sub>2</sub>F<sub>8</sub>) seems very promising.

## Funding

This work has received funding from the European Union's Horizon 2020 research and innovation programme under the Marie Skłodowska-Curie grant agreement No 657630. P.L. acknowledges financial support from the Government of the Russian Federation (Grant 074-U01) through ITMO Post-Doctoral Fellowship scheme.